Skeletal Radiol (2014) 43:1237–1246
DOI 10.1007/s00256-014-1923-5

SCIENTIFIC ARTICLE

Total hip prosthesis CT with single-energy projection-based metallic artifact reduction: impact on the visualization of specific periprosthetic soft tissue structures

Pedro Augusto Gondim Teixeira · Jean-Baptiste Meyer · Cedric Baumann · Ariane Raymond · François Sirveaux · Henry Coudane · Alain Blum

Received: 10 February 2014 / Revised: 22 April 2014 / Accepted: 19 May 2014 / Published online: 10 June 2014

Abstract
Objectives To compare the image quality of CT with iterative reconstruction alone and in association with projection-based single-energy metal artifact reduction (SEMAR) for the visualization of specific periarticular soft tissue structures in patients with hip prostheses.
Methods CT studies from 48 consecutive patients with a hip prosthesis (24 unilateral and 24 bilateral) were retrospectively reconstructed using two different methods: iterative reconstruction (IR) alone and IR associated with SEMAR. The influence of metallic artifacts on the identification of various periarticular structures was evaluated subjectively by two readers. The image quality was compared in patients with unilateral and bilateral prostheses.
Results Visualization of periprosthetic soft tissue was significantly improved by the SEMAR algorithm ($p<0.0001$). When SEMAR was associated with IR, the gluteus minimus and medius tendons, obturator internus muscle, prostate/uterus and bladder could be seen with medium or high confidence. There were no significant differences in image quality between patients with unilateral or bilateral prosthesis when SEMAR was used ($p>0.2$). This algorithm increased the detection of periarticular masses by 30 %.
Conclusion SEMAR significantly improves the image quality of periarticular soft-tissue structures in patients with hip prostheses.

Keywords Computed tomography · Hip arthroplasty · Image quality · Metal artifacts

This work was supported by a research grant from the French Society of Radiology (SFR, Societé Française de Radiologie).

P. A. Gondim Teixeira · J.-B. Meyer · A. Raymond · A. Blum
Service D'imagerie Guilloz, CHU-Nancy, Hôpital Central, 29, Av Marechal Lattre de Tassigny, 54035 Nancy, France

J.-B. Meyer
e-mail: meyerjeanbaptiste@hotmail.fr

A. Raymond
e-mail: ariane.raymond@gmail.com

A. Blum
e-mail: alain.blum@gmail.com

P. A. Gondim Teixeira
Université de Lorraine, IADI, UMR, S 947, Nancy, France

C. Baumann
Service d'épidemiologie et évaluation cliniques, CHU-Nancy, Av Marechal Lattre de Tassigny, 54035 Nancy, France
e-mail: c.baumann@chu-nancy.fr

F. Sirveaux
Service de Chirurgie Traumatologique et Orthopédique, Centre Chirurgical Emile Gallé, 54000 Nancy, France
e-mail: fsirveaux@sincal-cto.fr

H. Coudane
Service de Chirurgie traumatologique et arthroscopique de l'appareil locomoteur (ATOL), CHU-Nancy, Hôpital Central, 29, Av Marechal Lattre de Tassigny, 54035 Nancy, France
e-mail: henry.coudane@univ-lorraine.fr

P. A. Gondim Teixeira (✉)
42 Rond Point Kleber, Jarville-la-Malgrange, 54140 Nancy, France
e-mail: ped_gt@hotmail.com

Introduction

Total replacement surgery is often used to treat advanced degenerative joint disease of the hip [1]. Although complication rates are low, the large numbers of prostheses implanted mean that radiologists are likely to be confronted with post-surgical periprosthetic complications [2]. CT is currently used to evaluate bone and metal hardware complications of hip arthroplasty and is the only method available for bone stock analysis in patients evaluated for prosthetic replacement [3, 4]. Soft tissue complications after hip arthroplasty are less common than prosthetic loosening and displacement, but can cause significant patient disability. Multiple periarticular soft-tissue structures, such as gluteal tendons, the psoas tendon and sciatic nerve, can be implicated [5–7]. Although CT has an important role in post-arthroplasty evaluation, there is no evidence to support its use in diagnosing soft tissue complications.

Sonography is a valuable option for the post-surgical evaluation of periprosthetic soft tissues of the hip [1]. In the postoperative setting, however, sonographic evaluation can be hindered by post-surgical scarring, soft tissue calcifications and surgical material [8, 9]. Despite the use of adapted sequences and acquisition parameters, metallic artifacts still reduce the quality of MR images, thereby obscuring periprosthetic soft-tissue anomalies. In this context, techniques that improve imaging of soft tissue structures on CT could be important for patient care [1, 2].

The improvement of image quality using projection-based algorithms for metallic artifact reduction (MAR) in patients with metallic implants is well documented in the literature [10–14]. Various authors have demonstrated the positive impact of these techniques on the visualization of pelvic organs in patients with total hip prostheses. Yet despite the undisputed improvement in image quality achieved using projection-based MAR, various aspects of their application remain poorly understood. The diagnostic gain associated with visualization of specific periarticular soft tissue structures has not yet been directly evaluated in the literature. Projection-based MAR is frequently used in association with dual-energy, which can complicate the acquisition protocol and increase the radiation dose. Finally, the influence of the amount of metal on the performance of projection-based MAR algorithms also requires clarification.

In this investigation, we compared the image quality of CT with iterative reconstruction (IR) alone and in association with a SEMAR algorithm for the visualization of specific periarticular soft tissue structures in patients with hip prostheses. This information might be expected to help ascertain the role of CT with projection-based MAR in the diagnostic workup of patients with hip prostheses.

Material and methods

Patients

From July 2012 to April 2013, hip CT studies were performed on 48 consecutive patients with hip prostheses referred to our institution. Patients had been referred for the evaluation of hip pain after total hip arthroplasty; 24 had unilateral and 24 bilateral prostheses. Among the patients with bilateral prostheses, there were four hip arthrographies; these were excluded, giving a total of 68 hip prostheses available for evaluation. Raw data from the examinations were retrospectively retrieved. This study was approved by the local ethics committee, and all patients were over 18 years of age.

Informed consent is not required by the ethics committee of our institution for retrospective studies based on post-processing of anonymized data.

Acquisition protocol

All CT examinations were performed using a 320-detector-row CT scanner (Aquilion ONE, Toshiba Medical Systems, Otawara, Japan). A single volume with 16 cm of z-axis coverage was acquired in the sequential mode starting 3 cm proximal to the acetabular roof. The acquisition parameters were determined by the patient's body mass index: tube rotation time 0.75–1.0 s, 120–135 kVp, 100–450 mAs, slice thickness 0.5 mm, FOV 32 cm and matrix 512×512. In patients with bilateral prostheses, the acquisition volume was positioned to include both hips.

Image post-processing

Two volumes were reconstructed for each patient, one using an adaptive IR algorithm (AIDR 3D, Toshiba Medical Systems) and one using IR in association with a SEMAR algorithm (SEMAR, Toshiba Medical Systems). A standard soft tissue kernel (FC08) was used for all reconstructions. AIDR 3D is an adaptive noise-reduction algorithm that uses a combination of raw data and image-based reconstruction techniques that have been described previously [15, 16]. After data acquisition, the volume with IR only was automatically created by the scanner. Then the raw data were post-processed on an external workstation, research workstation V6.0 (Toshiba Medical Systems, Otawara, Japan) to be reconstructed with the SEMAR algorithm [17].

The SEMAR algorithm is shown in Fig. 1 and is summarized in the following steps:

1. Segmentation of metal parts in the iteratively reconstructed original image (first-pass image);
2. Forward reprojection of the metal image to find the metal trace in the sinogram;

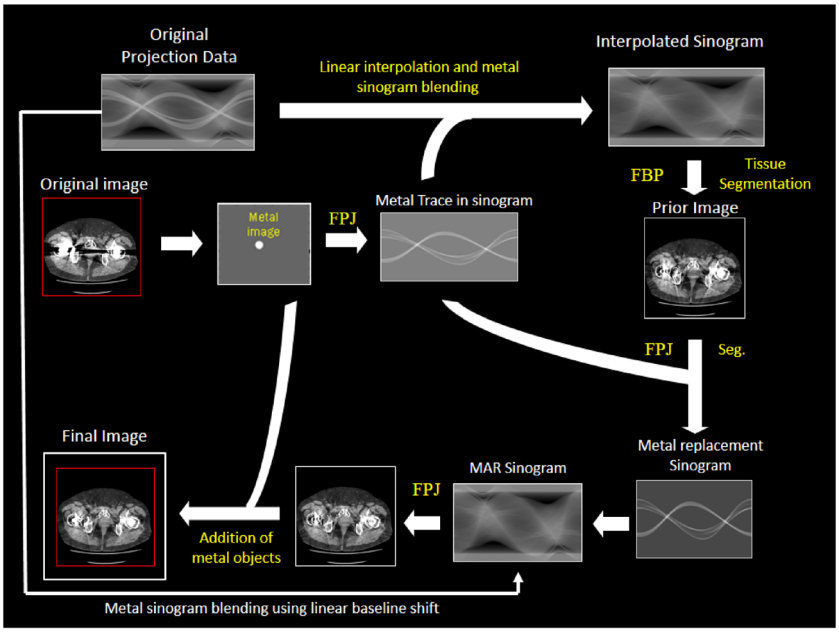

Fig. 1 Diagram demonstrating the multiple steps of the MAR algorithm used. *FPJ* = Forward projection; *FBP* = filtered back projection; *Seg* = segmentation of metallic artifacts in the image domain

3. Linear interpolation of the metal trace in the sinogram using the nearby measurements;
4. Reconstruction of the interpolated sinogram (second-pass image);
5. Segmentation of the interpolation-corrected image into various tissue classes [18];
6. Forward reprojection of the combined image onto the metal trace using linear integration of interpolated voxels [19];
7. Blending of the original sinogram with the forward reprojection of the tissue-classified image on the metal trace using a linear baseline shift approach;
8. Reconstruction of the sinogram (third-pass image);
9. Blending of the reconstructed image with the metal image to obtain the final image.

In step 1, the metal is differentiated on the original image using either a simple fixed threshold or an automatic threshold approach. Then, in step 2, the metal image is forward reprojected to find the metal trace in the sinogram. A pixel-driven projector is used to determine the region of the metal trace. Once the metal trace has been obtained by forward reprojecting the metal image (step 4), the metal-blocked part in the sinogram is linearly interpolated using the neighboring non-metal-blocked measurements. Next, the filled sinogram on the metal trace is reconstructed, resulting in the second-pass image.

The second-pass image is then classified into "air," "water" and "bone" by threshold differentiation to obtain a prior image, which is forward reprojected onto the metal trace to provide an estimate of the projection attributable to it. A ray driven forward reprojection is implemented using linear integration of interpolated voxels, which simulates a true line integral of an object. The forward reprojection of the prior image may be on a very different scale than the original sinogram because it is not water-calibrated, whereas the original sinogram may be. In addition, if the prior image is reconstructed on a small FOV that does not contain all the objects, the forward projection will have a different scale than the original sinogram. Therefore, in step 7, in order to blend the original sinogram with the reprojection on the metal trace, a linear baseline shift approach is used to linearly adjust the baseline of the forward projection so that it aligns with the original sinogram in the metal region. Finally, the sinogram with blended reprojection is fed to the reconstruction, leading to the third-pass image.

Image analysis

All images were analyzed independently by two musculoskeletal radiologists (P.T. and J.M.) with 8 and 4 years of clinical experience. The readers were blinded to clinical data. First, the IR-only volumes were evaluated on a display console workstation V4.74 (Toshiba Medical Systems, Otawara, Japan). Then, after a 2-week interval, the IR associated with SEMAR volumes was evaluated in the same manner. Images were analyzed in the axial plane with a 40/400 HU window width/level setting.

The influence of metallic artifacts on the visualization of multiple soft-tissue periprosthetic structures was graded as follows: 0 = structure completely obscured; 1=marked artifacts with questionable recognition; 2=faint anatomic recognition; 3=recognition with low confidence; 4=recognition with medium confidence; 5=recognition with high confidence [11]. Seven soft tissue structures were evaluated in each patient: gluteus minimus tendon, gluteus medius tendon, ilio-psoas

tendon, sciatic nerve, obturator internus muscle, bladder and uterus/prostate. Although the bladder and uterus/prostate are not usually involved in post-arthroplasty complications, they were included in the analysis to allow for comparison between the results obtained and findings in the literature. All slices depicting a given structure were analyzed in the axial plane. The slice that depicted the most prominent metallic artifacts over each structure was chosen for grading. Slices were selected by each reader independently. A global visualization score ranging from 0 to 35 comprising the sum of the grades for each structure was calculated for each prosthesis. In patients with bilateral prostheses, the image quality was evaluated independently on each side and was based only on analysis of the specific anatomical structures described above (as opposed to a global image aspect).

The readers also assessed the presence of periprosthetic masses characterized by the identification of a space-occupying anomaly of soft-tissue density clearly distinct from periarticular anatomic structures. Only anomalies over 1.0 cm in the greatest diameter were considered for evaluation. The influence of the metallic artifacts on the visualization of these abnormalities was classified in the same manner as previously described. When visible, the appearance of gluteus medius and minimus tendons was classified as normal, tendon thickening and tendon discontinuity. Normal tendons were characterized by well-defined tendon contours and a homogeneous thickness throughout their length. Thickened tendons were characterized by an abrupt variation in tendon width and abnormal tendon contours. Tendon discontinuity was characterized by a loss of visualization of the tendon fibers.

The volume computed tomography dose index ($CTDI_{vol}$) and the global dose length product (DLP) were estimated based on a 32-cm phantom. Effective dose estimations were obtained with a constant (k-factor) in $mGy*cm*mSv^{-1}$of 0.0073 for the hip [20].

Statistics

The paired two-tailed Student's *t* test was used to compare quality scores. The non-paired Student's *t* test was used to compare quality scores between patients with unilateral and bilateral prostheses. The ANOVA test was used to compare image quality between the different types of prosthesis. A p value of less than 0.05 was considered as the threshold of statistical significance. Intra-class correlation coefficients were calculated to assess inter-observer variability.

Results

There were 25 males and 23 females in the population studied (male: ratio=1:0.92). Age ranged from 26 to 90 years (mean=66.7±14.9 years). The mean ages among patients with unilateral and bilateral prosthesis were almost identical (66.6±14.8 and 66.8±15.3 years, respectively). Body mass index (BMI) was also similar (27.7±4.6 and 26.3±5.7, respectively). There were 66 total hip prostheses (THPs) and two bipolar hemiarthroplasties. Among the THPs evaluated there were 40 metal-on-polyethylene bearings, 12 ceramic-on-ceramic bearings, 6 ceramic-on-polyethylene bearings and 8 metal-on-metal bearings. Six prostheses did not have a metal back on the acetabular component. There were no resurfacing prostheses in the studied population.

Visualization of periprosthetic soft tissue was significantly improved by the SEMAR algorithm for both readers. Interobserver agreement was considered to be excellent with both reconstruction types (Intra class correlation coefficient= 0.91). The mean global score using IR alone was 8.5±6.6 and 6.4±5.6 for readers 1 and 2, respectively. When the SEMAR algorithm was used, the mean global scores were significantly higher at 28.0±4.4 and 26.8±4.5, respectively ($p<0.0001$).

The influence of metallic artifacts on image analysis varied depending on the anatomic structure evaluated. Table 1 presents the structure-specific scores for both readers. Analysis of the image quality scores of both readers allows some observations to be made. When IR alone was used, at least part of the obturator internus muscle, ilio-psoas tendon and bladder was completely obscured by the metallic artifacts; anatomic recognition of the gluteus minimus and medius tendons and the sciatic nerve was graded as questionable; faint recognition of the prostate/uterus was possible. When IR was associated with SEMAR, these structures (gluteus minimus and medius tendons, the obturator internus muscle, the protate/uterus and the bladder) could be seen with medium or high confidence (mean quality scores varied from 3.8 to 4.8) (Figs. 2, 3 and 4). Despite the positive effect of SEMAR visualization of the ilio-psoas tendon, the sciatic nerve remained difficult (mean quality scores varied from 2.2 to 3.6) (Figs. 5 and 6). Recognition of the ilio-psoas tendon was considered faint, and the sciatic nerve was recognized only with low confidence. Based on

Table 1 Mean quality scores per structure for both readers using IR and projection MAR

	IR only		Projection MAR	
Anatomic structure	Reader 1	Reader 2	Reader 1	Reader 2
Gluteus minimus tendon	1.3±1.4	1.0±1.2	4.2±1.1	3.8±1.3
Gluteus medius tendon	1.6±1.5	1.0±1.4	4.7±0.6	4.3±0.8
Sciatic nerve	1.6±1.8	1.3±1.5	3.6±1.5	3.6±1.6
Obturator internus muscle	0.7±1.3	0.3±0.9	4.5±1.0	4.2±1.0
Ilio-psoas tendon	0.2±0.6	0.2±0.7	2.2±1.7	2.5±1.5
Prostate/uterus	2.0±2.2	1.7±1.9	4.8±0.5	4.4±0.7
Bladder	0.9±1.7	0.6±1.3	4.0±1.3	4.0±1.2
Gobal mean	1.22	0.92	4.02	3.86

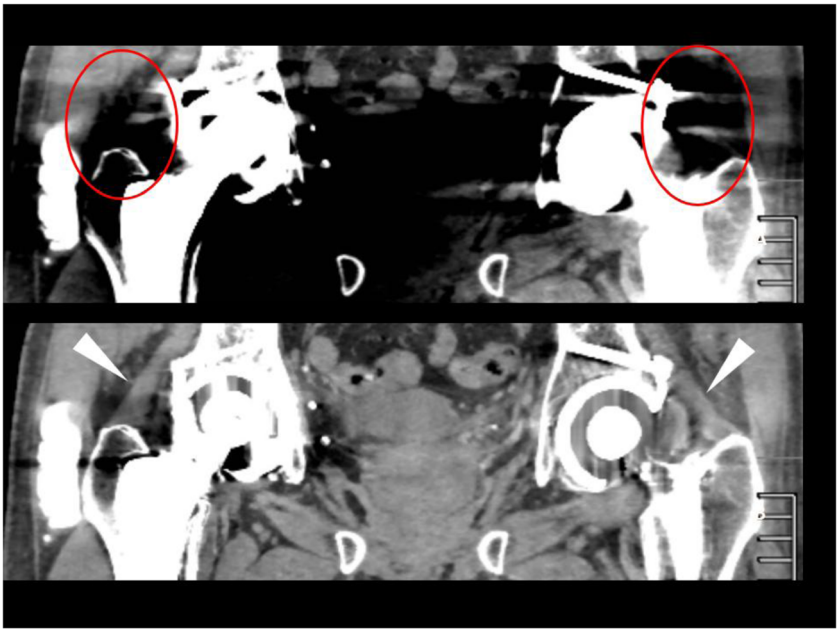

Fig. 2 A 54-year-old male with bilateral metal on polyethylene THP. **a** Coronal CT image at the level of the gluteal minimus tendons with IR-only reconstruction using a soft tissue window level (400/40 HU). Note the prominent metallic artifact that completely obscures these tendons (*red circles*). **b** Coronal CT image of the same anatomic region, with the same window settings using projection MAR. The image quality is significantly improved, and the gluteal minimus tendons can now be identified with high confidence (*arrowheads*). Note that compared to the opposite side, the left tendon appears thickened

these results, some practical recommendations are proposed in Table 2.

Use of SEMAR allowed the identification of more periarticular masses. The maximal diameters of these masses ranged from 1.5 to 8.1 cm (mean=3.4±1.4 cm). Their distance from the prostheses varied from 0 to 6.7 cm (mean=1.4 ±1.7 cm). On IR-only images, 14 and 13 masses were identified by readers 1 and 2, respectively. On SEMAR reconstructed images the numbers increased to 20 and 19, respectively, corresponding to increases of 30 % and 31.5 % in the detection rate. An increase in the diagnostic confidence of these anomalies was also noted when SEMAR was associated with IR (Fig. 7). The mean grade of these lesions for reader 1 was 3.3±1.5 and 4.7±0.5 with and without SEMAR, respectively. For reader 2 these values were 3.4±1.1 and 4.7±0.4.

Regarding the gluteal tendons, there was a large increase in the detection of apparent pathology (thickening or discontinuity) with the use of the SEMAR algorithm. Readers 1 and 2 identified 13 and 10 pathologic gluteus minimus tendons and 7 and 5 pathologic gluteus medius tendons using IR-only images, respectively. With SEMAR readers 1 and 2 identified 41 and 39 pathologic gluteus minimus tendons and 26 and 20 pathologic gluteus medius, respectively. This represents

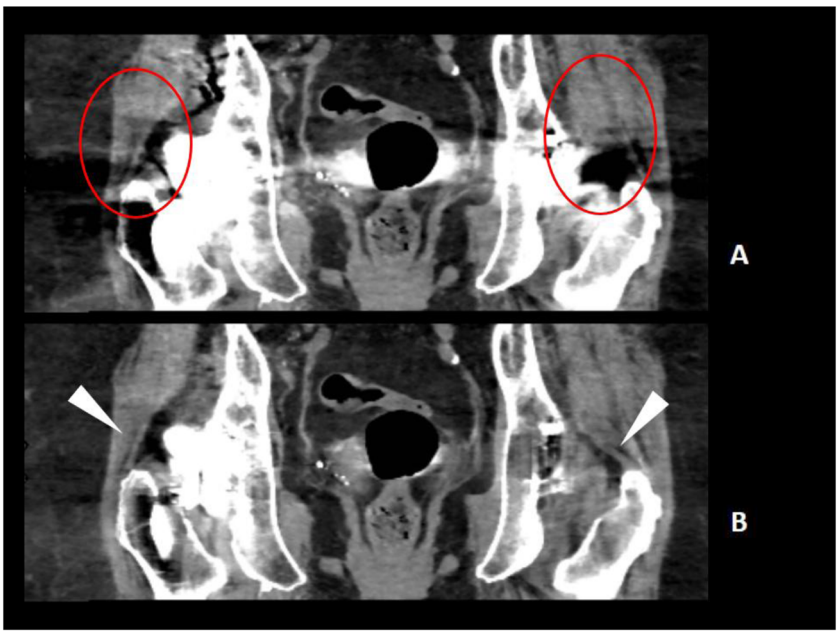

Fig. 3 A 77-year-old female with bilateral metal on polyethylene THP. **a** Coronal CT image at the level of the gluteal medius tendons with IR-only reconstruction using a soft tissue window level (400/40 HU). Note the prominent metallic artifact that completely obscures these tendons (*red circles*). **b** Coronal CT image of the same anatomic region, with the same window settings using projection MAR. The image quality is significantly improved, and the gluteal medius tendons can now be identified with high confidence (*arrowheads*). Note that there is an asymmetry of the myotendinous junction of these tendons. On the right the tendon appears longer, which can be related to partial tearing

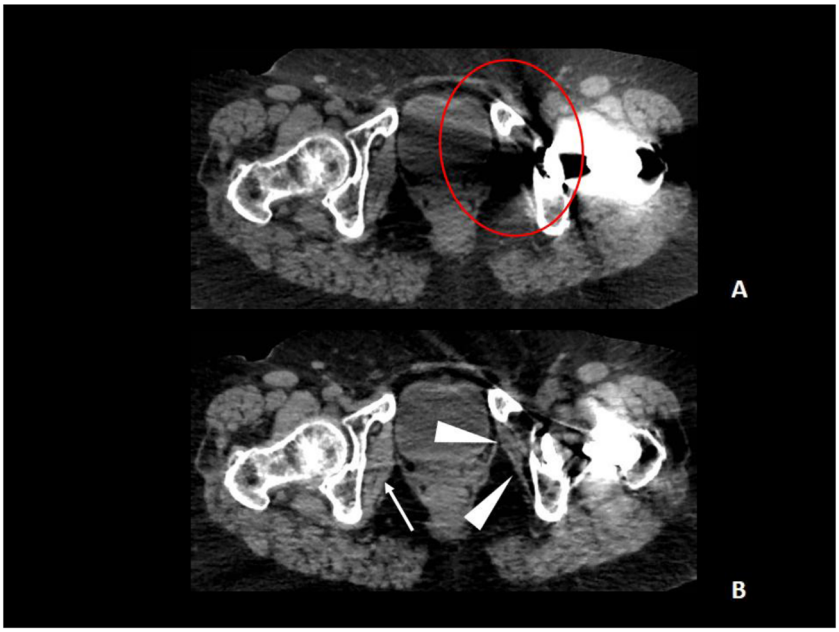

Fig. 4 A 70-year-old female with a left-sided metal on polyethylene THP. **a** Axial CT image reconstructed with IR only. Metal artifacts preclude analysis of the ipsilateral internal obturator muscle (*red circle*). **b** Axial CT image of the same anatomic region, with the same window level (400/40 HU) using projection MAR in which the internal obturator muscle is identified with high confidence. In this case compared to the contralateral muscle (*thin arrow*), the left internal obturator muscle shows a loss in volume and a few areas of fatty atrophy

increases of 68.2–74 % and 73–75 % in the detection of an abnormal appearance of gluteus minimus and medius tendons.

There was a significant drop in the quality of IR-only images in patients with bilateral prostheses when compared to patients with unilateral prostheses ($p<0.0001$ for both readers). The mean overall quality scores in patients with unilateral prostheses were 14.5±6.1 and 11.4±5.3 for readers 1 and 2. The mean overall quality scores in patients with bilateral prostheses were 5.2±4.0 and 3.7±3.5 for readers 1 and 2. With the use of the SEMAR algorithm, there were no significant differences in the image quality between patients with unilateral or bilateral prostheses ($p>0.2$ for both readers). With SEMAR reconstructed images, the mean overall quality scores in patients with unilateral prostheses were 28.8±4.6 and 27.4±4.9 for readers 1 and 2. The mean overall quality scores in patients with bilateral prostheses were 27.5±4.3 and 26.4±4.3 for readers 1 and 2.

There was no significant difference in the image quality scores in the different THP types on images reconstructed with SEMAR ($p=0.158$ for reader 1 and 0.824 for reader 2).

The mean CTDIvol, DLP and effective dose delivered to the patients evaluated were 32.5±19.9 mGy, 520.0±318.8 mGy*cm and 3.7±2.3 mSv. Exposure was lower in patients with unilateral THP. Table 3 presents the mean values

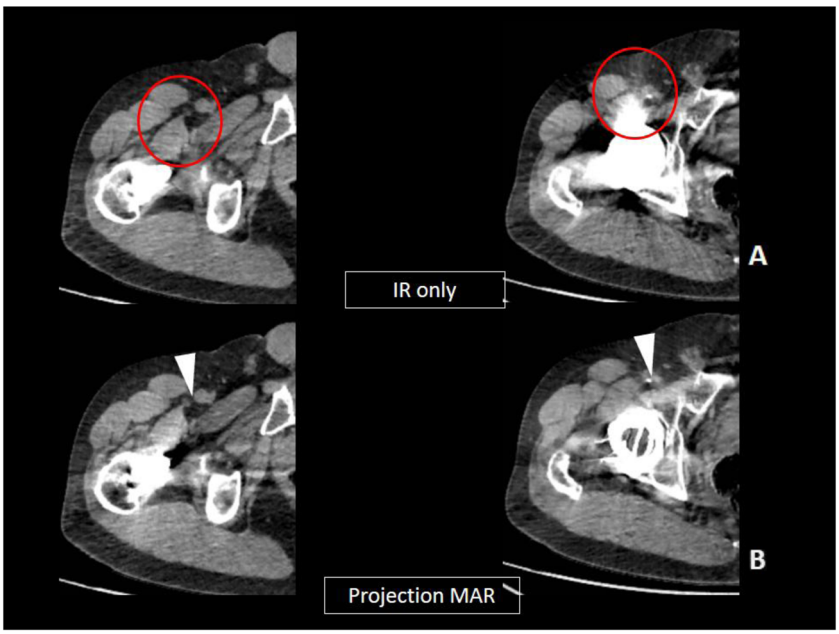

Fig. 5 A 52-year-old male with a right-sided ceramic on polyethylene THP. Two pairs of axial CT images from distal and proximal portions of the ilio-psoas tendon at the level of the proximal thigh with IR only (**a**) and with projection MAR (**b**). The same window level has been used (400/40). The *red circles* in **a** mark the expected position of the ilio-psoas tendon, which is completely obscured by the metallic artifacts. In **b** the distal portion of this tendon can be identified with high confidence (*arrowhead in the right image*); however, at the level of the acetabular cup this tendon is only faintly recognized (*arrowhead in the left image*)

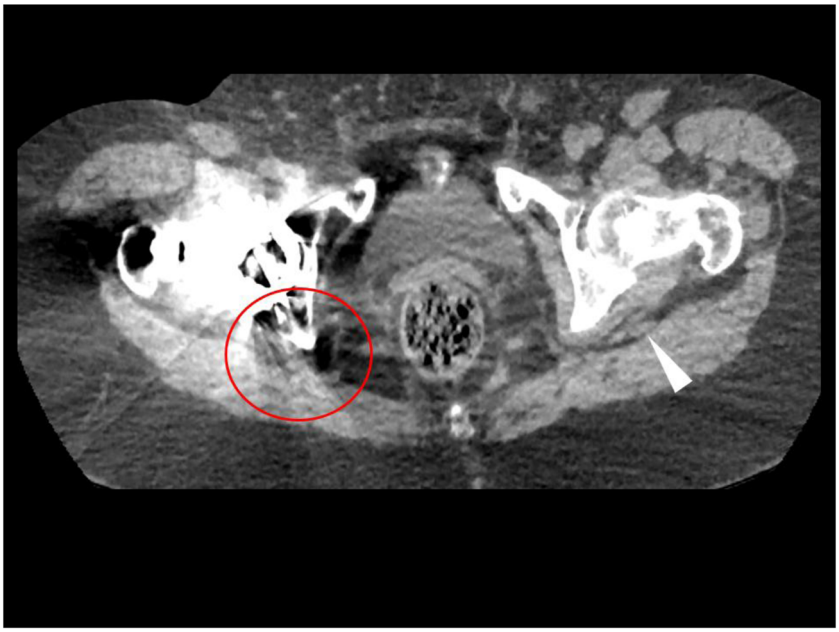

Fig. 6 A 52-year-old male with a right-sided ceramic on polyethylene THP. Axial CT images with projection MAR reconstruction with soft tissue windowing (400/10 HU). The residual metallic artifacts hinder identification of the sciatic nerve, which is only faintly recognized (*red circle*). The contralateral sciatic nerve is indicated by the white *arrowhead*

of CTDIvol and DLP and the effective dose for patients with unilateral and bilateral THP.

Discussion

The use of IR has been shown to improve image quality in patients with metallic implants [21]. The present results indicate that despite these improvements, the visualization of periprosthetic soft tissue structures using adaptive IR alone remains greatly hampered by metallic artifacts. The anatomic structures evaluated (gluteal tendons, ilio-psoas tendon, obturator internus muscle, sciatic nerve, uterus/prostate and bladder) were at best faintly recognized with IR-only images. The analysis of the ilio-psoas tendon, anterior and in close proximity to the acetabular component, and the obturator internus muscle medial to the prosthetic femoral head using this type of reconstruction was particularly hindered (mean scores 0.2 and 0.3–0.7, respectively). Thus, CT with IR alone cannot be recommended for the evaluation of periarticular soft tissue complications of hip arthroplasty.

Use of the SEMAR algorithm in association with IR significantly improved the image quality ($p<0.0001$). With SEMAR, analysis of the gluteal tendons and the obturator internus muscle was possible with medium to high confidence (mean quality scores ranged from 3.8 to 4.7). Although

Table 2 Structure-specific recommendations for each type of reconstruction used

	Recommendations	
Anatomic structure	IR only	IR with SEMAR
Gluteus minimus tendon	Visualization severely hampered by metallic artifacts	Recognition with medium/high confidence, CT can be considered for evaluation
Gluteus medius tendon	Visualization severely hampered by metallic artifacts	Recognition with medium/high confidence, CT can be considered for evaluation
Sciatic nerve	Visualization severely hampered by metallic artifacts	Visualization hampered by metallic artifacts but can be recognized in some patients
Obturator internus muscle	Completely obscured by metallic artifacts	Recognition with medium/high confidence, CT can be considered for evaluation
Ilio-psoas tendon	Completely obscured by metallic artifacts	Visualization hampered by metallic artifacts but can be recognized in some patients
Prostate/uterus	Visualization hampered by metallic artifacts but can be recognized in some patients	Recognition with medium/high confidence, CT can be considered for evaluation
Bladder	Completely obscured by metallic artifacts	Recognition with medium/high confidence, CT can be considered for evaluation

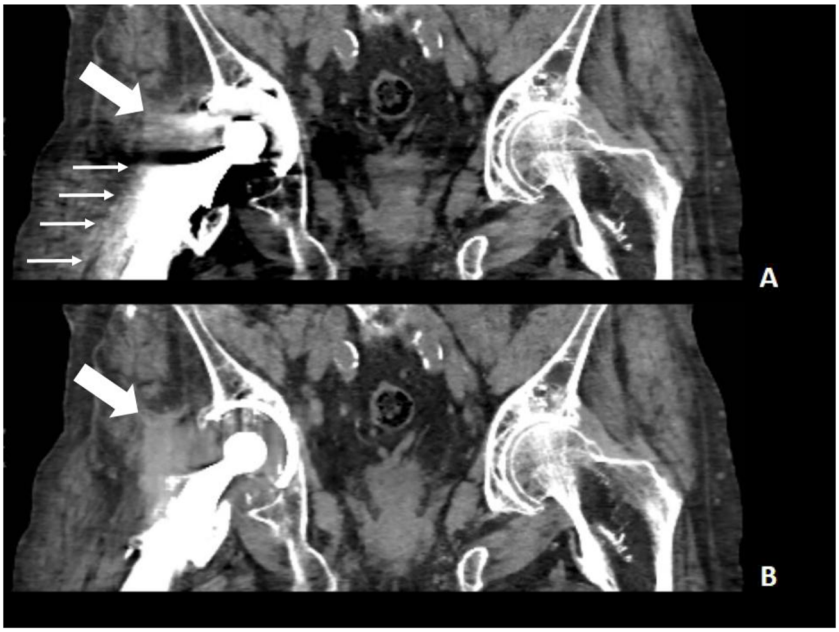

Fig. 7 A 74-year-old male with bilateral metal on polyethylene THP. **a** Coronal CT image with IR-only reconstruction using a soft tissue window level (400/40 HU) demonstrating a periarticular soft tissue mass (*fat arrow*), which is partially obscured by metallic artifacts (*thin arrows*). **b** Coronal CT image of the same anatomic region with the same window settings using projection MAR. The image quality is significantly improved, and the periarticular soft tissue mass (*fat arrow*) can be identified with high confidence. On **b**, this mass seems to be continuous with the articular cavity, a feature that can have important diagnostic implications

significantly improved by SEMAR, the image quality of the ilio-psoas tendon and sciatic nerve remained mediocre. These findings are probably related to the proximity to metallic prosthetic components. The mean quality grade of these structures varied from 2.2 to 3.6. Thus, CT with the presented MAR algorithm can be used to evaluate periarticular soft tissue structures in patients with THP, particularly the gluteal tendons and obturator internus muscle.

Multiple investigations demonstrate the benefits of using projection-based MAR, but information on the clinical importance of these techniques is scarce [22–24]. The MAR algorithm used here led to a 30 % increase in the rate of detection of periarticular masses. Not only did both readers identify more lesions, but confidence in the analysis of these anomalies was also improved (quality scores 3.3–3.4 and 4.7 for IR-only and SEMAR reconstructions, respectively). There was also a large increase in the identification of morphologic anomalies of the gluteus minimus and medius tendons (68–75 %). These results indicate that the use of SEMAR increases the performance of CT for the diagnosis of periprosthetic soft tissue anomalies in patients with THP.

Table 3 Dose exposure levels in the studied population

		CTDIvol (mGy)	DLP (mGy[a]cm)	Effective dose (mSv)
Uni lat	Mean	26.6	425.3	3.1
	SD	19.1	306.9	2.2
Bilat	Mean	38.4	614.8	4.4
	SD	19.2	307.6	2.2
Global	Mean	32.5	520	3.7
	SD	19.9	318.7	2.3

The impact of the number of prostheses on image quality has not been previously assessed in the literature. On IR-only images, there was a significant degradation of image quality in patients with bilateral hip prostheses. The global quality score for IR alone was 11–14 for unilateral prostheses versus 3–5 for bilateral implants. However, when the SEMAR algorithm was applied, this degradation was less important. Actually, the image quality assessment was not statistically different in the two groups (27–28 versus 26–27 for unilateral and bilateral prostheses, respectively), which indicates that this technique is particularly useful when large amounts of metal are present.

In most studies, projection-based MAR has been used in association with dual-energy techniques (monochromatic imaging). Using the same grading system and dual-energy monochromatic imaging associated with a projection-based MAR algorithm, Morsbach et al. reported a median score of 3 for the prostate and bladder [11]. Still using the same scoring system, Yu et al. also reported similar results using a single-energy projection-based MAR (3.3 and 3.4 for the bladder and prostate, respectively) [25]. The score for these structures using the present MAR algorithm was slightly better and varied from 4 to 4.8 in the population studied.

One theoretical advantage of dual-energy monochromatic imaging over SEMAR is that the latter introduces morphologic alterations to metal and/or periprosthetic bone and thus should be reserved for the evaluation of soft tissue structures. Some drawbacks of dual-energy-based MAR techniques have to be acknowledged. There is no consensus in the literature about the optimal kVp for dual-energy MAR protocols [26]. Additionally, various factors, such as the patient size, prosthesis composition

and dual-energy acquisition method (e.g., dual source, sandwich detectors, rapid kV switching), may influence the effectiveness of dual-energy MAR [26, 27]. With a similar performance, SEMAR allows simpler acquisition protocols and is potentially applicable in all scanner models [13]. Additionally, SEMAR techniques can lower the dose delivered to the patient.

Various limitations of this study should be acknowledged. Only the image quality improvement and not the diagnostic performance of the MAR techniques was assessed. We had no diagnostic confirmation of the capsular and periarticular anomalies identified. Nonetheless, the high interobserver agreement helps support the validity of these findings. Although pathologic aspects of the structures evaluated were found in several of the cases analyzed, the lack of a gold standard precluded the evaluation of the diagnostic performance of the SEMAR algorithm. Various prosthesis types were present in the study population, and the number of patients with each specific prosthesis type was limited. The influence of the metal alloy used in the prosthesis evaluated was not assessed. Although the metal alloy of which the prostheses is made certainly has an influence on the effectiveness of MAR algorithms, in our clinical practice only the amount of metal had a noticeable effect on the quality of the SEMAR reconstructed images.

In conclusion, CT images with IR alone yielded poor visualization of the periprosthetic soft tissues in patients with hip arthroplasty. The association of IR with the SEMAR algorithm led to significant improvement in quality, even in patients with bilateral prostheses. When this algorithm was used, the gluteal tendons and obturator internus muscle could be visualized with medium to high confidence. Moreover, there was an increase in the rate of detection of periarticular masses and gluteal tendon morphologic changes, suggesting that the MAR algorithm used may be of value in the postoperative evaluation of patients with total hip arthroplasty.

Acknowledgments This work was supported by a research grant from the French Society of Radiology (SFR, Société Française de Radiologie). We thank Valerie Lamy and Laurent Raffray for their efforts in data transfer and post-processing.

Conflict of interest The authors declare that they have no conflict of interest.

Disclosures Two authors involved in this work, myself included (P.T. and A.B..), participate in a non-remunerated research contract with Toshiba Medical systems, developer of the algorithm used for metal artifact reduction. The other authors have no potential conflicts of interest to disclose.

References

1. Miller TT. Imaging of hip arthroplasty. Eur J Radiol. 2012;81:3802–12.
2. Roth TD, Maertz NA, Parr JA, Buckwalter KA, Choplin RH. CT of the hip prosthesis: appearance of components, fixation, and complications. Radiogr Rev Publ Radiol Soc North Am Inc. 2012;32:1089–107.
3. Cahir JG, Toms AP, Marshall TJ, Wimhurst J, Nolan J. CT and MRI of hip arthroplasty. Clin Radiol. 2007;62:1163–71. discussion 1172–1173.
4. Choplin RH, Henley CN, Edds EM, Capello W, Rankin JL, Buckwalter KA. Total hip arthroplasty in patients with bone deficiency of the acetabulum. Radiogr Rev Publ Radiol Soc North Am Inc. 2008;28:771–86.
5. Bremer AK, Kalberer F, Pfirrmann CWA, Dora C. Soft-tissue changes in hip abductor muscles and tendons after total hip replacement: comparison between the direct anterior and the transgluteal approaches. J Bone Joint Surg (Br). 2011;93:886–9.
6. Henderson RA, Lachiewicz PF. Groin pain after replacement of the hip: aetiology, evaluation and treatment. J Bone Joint Surg (Br). 2012;94:145–51.
7. Park JH, Hozack B, Kim P, Norton R, Mandel S, Restrepo C, et al. Common peroneal nerve palsy following total hip arthroplasty: prognostic factors for recovery. J Bone Joint Surg Am. 2013;95:e551–5.
8. Douis H, Dunlop DJ, Pearson AM, O'Hara JN, James SLJ. The role of ultrasound in the assessment of post-operative complications following hip arthroplasty. Skeletal Radiol. 2012;41:1035–46.
9. Long SS, Surrey D, Nazarian LN. Common sonographic findings in the painful hip after hip arthroplasty. J Ultrasound Med Off J Am Inst Ultrasound Med. 2012;31:301–12.
10. Kalender WA, Hebel R, Ebersberger J. Reduction of CT artifacts caused by metallic implants. Radiology. 1987;164:576–7.
11. Morsbach F, Bickelhaupt S, Wanner GA, Krauss A, Schmidt B, Alkadhi H. Reduction of metal artifacts from hip prostheses on CT images of the pelvis: value of iterative reconstructions. Radiology. 2013;268:237–44.
12. Lee YH, Park KK, Song H-T, Kim S, Suh J-S. Metal artefact reduction in gemstone spectral imaging dual-energy CT with and without metal artefact reduction software. Eur Radiol. 2012;22:1331–40.
13. Yu L, Leng S, McCollough CH. Dual-energy CT-based monochromatic imaging. AJR Am J Roentgenol. 2012;199:S9–15.
14. Brook OR, Gourtsoyianni S, Brook A, Mahadevan A, Wilcox C, Raptopoulos V. Spectral CT with metal artifacts reduction software for improvement of tumor visibility in the vicinity of gold fiducial markers. Radiology. 2012;263:696–705.
15. Yang Z, Silver MD, Noshi Y. Effective Data-domain Noise and Streak Reduction for X-Ray CT. 11th International Meeting on Fully Three-Dimensional Image Reconstruction in Radiology and Nuclear Medicine, Potsdam, Germany; 2011.
16. Yang Z, Zamyatin A, Akino N. Adaptive Weighted Anisotropic Diffusion For Computed Tomography Denoising. 11 th International Meeting on Fully Three-Dimensional Image Reconstruction in Radiology and Nuclear Medicine, Potsdam, Germany; 2011.
17. Chang Y-B, Xu D, Zamyatin A. Metal Artifact Reduction Algorithm for Single Energy and Dual Energy CT scans. 2012 I.E. Nucl. Sci. Symp. Med. Imaging Conf. Rec. 16/112012;3426–9.
18. Bal M, Spies L. Metal artifact reduction in CT using tissue-class modeling and adaptive prefiltering. Med Phys. 2006;33:2852–9.
19. Joseph PM. An improved algorithm for re projecting rays through pixel images. IEEE Trans Med Imaging. 1982;1:192–6.
20. Biswas D, Bible JE, Bohan M, Simpson AK, Whang PG, Grauer JN. Radiation exposure from musculoskeletal computerized tomographic scans. J Bone Joint Surg Am. 2009;91:1882–9.
21. Gervaise A, Osemont B, Lecocq S, Noel A, Micard E, Felblinger J, et al. CT image quality improvement using adaptive iterative dose reduction with wide-volume acquisition on 320-detector CT. Eur Radiol. 2012;22:295–301.

22. Lee YH, Park KK, Song H-T, Kim S, Suh J-S. Metal artefact reduction in gemstone spectral imaging dual-energy CT with and without metal artefact reduction software. Eur Radiol. 2012;22: 1331–40.
23. Malan DF, Botha CP, Kraaij G, Joemai RMS, van der Heide HJL, Nelissen RGHH, et al. Measuring femoral lesions despite CT metal artefacts: a cadaveric study. Skeletal Radiol. 2012;41:547–55.
24. Verburg JM, Seco J. CT metal artifact reduction method correcting for beam hardening and missing projections. Phys Med Biol. 2012;57:2803–18.
25. Yu L, Li H, Mueller J, Kofler JM, Liu X, Primak AN, et al. Metal artifact reduction from reformatted projections for hip prostheses in multislice helical computed tomography: techniques and initial clinical results. Invest Radiol. 2009;44:691–6.
26. Yu L, Christner JA, Leng S, Wang J, Fletcher JG, McCollough CH. Virtual monochromatic imaging in dual-source dual-energy CT: radiation dose and image quality. Med Phys. 2011;38:6371–9.
27. Vrtiska TJ, Takahashi N, Fletcher JG, Hartman RP, Yu L, Kawashima A. Genitourinary applications of dual-energy CT. AJR Am J Roentgenol. 2010;194:1434–42.